PHYSICS OF FLUIDS **25**, 024101 (2013)

Dissolution-driven convection in a Hele–Shaw cell

Anja C. Slim,[1,a)] M. M. Bandi,[1,b)] Joel C. Miller,[2,c)] and L. Mahadevan[1,3,d)]
[1]*School of Engineering and Applied Sciences, Harvard University, 29 Oxford Street, Cambridge, Massachusetts 02138, USA*
[2]*Harvard School of Public Health, 667 Huntington Avenue, Boston, Massachusetts 02115, USA*
[3]*Department of Physics, Harvard University, 29 Oxford Street, Cambridge, Massachusetts 02138, USA*

(Received 6 January 2012; accepted 26 November 2012; published online 15 February 2013)

Motivated by convection in the context of geological carbon-dioxide (CO_2) storage, we present an experimental study of dissolution-driven convection in a Hele–Shaw cell for Rayleigh numbers $\mathcal{R}$ in the range $100 < \mathcal{R} < 1700$. We use potassium permanganate ($KMnO_4$) in water as an analog for CO_2 in brine and infer concentration profiles at high spatial and temporal resolution and accuracy from transmitted light intensity. We describe behavior from first contact up to 65% average saturation and measure several global quantities including dissolution flux, average concentration, amplitude of perturbations away from pure one-dimensional diffusion, and horizontally averaged concentration profiles. We show that the flow evolves successively through distinct regimes starting with a simple one-dimensional diffusional profile. This is followed by linear growth in which fingers are initiated and grow quasi-exponentially, independently of one-another. Once the fingers are well-established, a flux-growth regime begins as fresh fluid is brought to the interface and contaminated fluid removed, with the flux growing to a local maximum. During this regime, fingers still propagate independently. However, beyond the flux maximum, fingers begin to interact and zip together from the root down in a merging regime. Several generations of merging occur before only persistent primary fingers remain. Beyond this, the reinitiation regime begins with new fingers created between primary existing ones before merging into them. Through appropriate scaling, we show that the regimes are universal and independent of layer thickness (equivalently $\mathcal{R}$) until the fingers hit the bottom. At this time, progression through these regimes is interrupted and the flow transitions to a saturating regime. In this final regime, the flux gradually decays in a manner well described by a Howard-style phenomenological model.
 [http://dx.doi.org/10.1063/1.4790511]

I. INTRODUCTION

Geological carbon-dioxide storage has the potential to be a near-term implementable technology that diverts atmosphere-bound anthropogenic CO_2 emissions into underground storage.[1] The proposal is to capture CO_2 from point sources (e.g., fossil-fuel burning power stations), purify it, compress it, and store it at depths of 1 to 3 km beneath the Earth's surface. At this depth, the (supercritical) CO_2 (of density 600 to 700 kg m^{-3}) is positively buoyant relative to resident brine (of density $\sim$ 1000 kg m^{-3}). The CO_2 rises through permeable rock until it reaches an impermeable barrier, along which it spreads laterally to form a roughly horizontal pool of CO_2 overlying brine. Being

[a)]Present address: Schlumberger–Doll Research, 1 Hampshire Street, Cambridge, Massachusetts 01239, USA.
[b)]Present address: Collective Interactions Unit, OIST Graduate University, 1919-1 Tancha, Onna-son, Okinawa 904-0495 Japan.
[c)]Present address: Departments of Mathematics and Biology, Penn State University, University Park, State College, Pennsylvania 16802, USA.
[d)]Corresponding author: lm@seas.harvard.edu.

slightly soluble, CO_2 then gradually dissolves into the surrounding brine, initially purely through diffusion, to generate a layer of brine containing aqueous CO_2 at the interface. Upon achieving sufficient thickness, this negatively buoyant layer becomes gravitationally unstable and convective overturning commences.[2,3] By forcing fresher fluid to the CO_2-brine interface and thus sharpening concentration gradients, convection substantially enhances the dissolution flux.

Here we study the dissolution process from first contact between CO_2 and brine through to almost complete saturation. Because the subsurface geological conditions are not readily simulated in a laboratory, we use an analog experiment in a Hele–Shaw cell with an idealized geometry of a horizontal boundary between solute and water and a horizontal, impermeable lower boundary. As our solute we use potassium permanganate ($KMnO_4$), which closely mimics relevant CO_2 properties and for which we can readily infer concentration from color intensity. The relevant dimensionless parameter for this process is the Rayleigh number

$$\mathcal{R} = \frac{HK\Delta\rho g}{\phi D\mu}, \tag{1}$$

where $K = d^2/12$ is the effective permeability with d the Hele–Shaw cell gap size, $\phi = 1$ is the effective porosity, $\Delta\rho = \rho_{\text{sat}} - \rho_0$ is the excess density of $KMnO_4$-saturated water (of density ρ_{sat}) over pure water (of density ρ_0), μ viscosity, D diffusivity, g gravity, and H the cell height. We present results for $100 < \mathcal{R} < 1700$.

Before we describe our study, it is useful to compare and contrast recent studies investigating convection in this context. On the experimental side, Kneafsey and Pruess[4] presented results for $\mathcal{R} = 40$, 75, and 370 for CO_2 and water at 4 MPa in a Hele–Shaw cell and quasi-2D porous medium. They reported onset of convection, measured by the flux beginning to deviate from pure diffusion, as the dimensional time $(\phi\mu/K\Delta\rho g)^2 D t_{\text{flux}}$, with $48 < t_{\text{flux}} < 177$ (note that t_{flux} is dimensionless in the advection–diffusion scalings of Sec. II). In the large $\mathcal{R}$ limit, Neufeld *et al.*[5] investigated behavior for $5 \times 10^4 < \mathcal{R} < 6 \times 10^5$ in a quasi-2D porous medium and Backhaus *et al.*[6] considered convection for $6000 < \mathcal{R} < 9 \times 10^4$ in a Hele–Shaw cell. Both studies used pairs of fully miscible fluids that have a density maximum at an intermediate mixing ratio. Both observed and focused on an intermediate-time regime in which the dissolution flux appears steady. They found that a dimensionless measure of the mass flux characterized by the Sherwood number $\mathcal{S}$ follows $\mathcal{S} = 0.12\mathcal{R}^{-0.16}$ and $\mathcal{S} = (0.045 \pm 0.025)\mathcal{R}^{-0.24\pm0.06}$, respectively, where

$$\mathcal{S} = \frac{\mu}{K\Delta\rho g c_{\text{sat}}} F, \tag{2}$$

with F the mass flux and c_{sat} the mass of solute per unit volume of saturated solution. Backhaus *et al.*[6] also described the dynamics of finger merging and reinitiation and reported wavenumber selection in time. Related experiments on finger formation in miscible Rayleigh–Taylor mixing are described by Wooding[7] and Fernandez *et al.*[8]

On the theoretical side, several studies have focused on predicting convective onset for the same idealized geometry that we consider (see Rees *et al.*[9] for a review). Studying onset is challenging because the base state of pure diffusion evolves in time and so standard linear stability approaches are inapplicable. A lower bound for the time at which perturbations can grow (the first time at which the mean-square difference between the observed distribution of dissolved CO_2 and the pure diffusion solution can grow) is provided by Slim and Ramakrishnan.[10] For $\mathcal{R} < 32.50$, convection is impossible. For $\mathcal{R} \geq 32.50$, onset occurs after a dimensional time $(\phi\mu/K\Delta\rho g)^2 D t_{\text{amp}}$, where $t_{\text{amp}} = 110$ for $\mathcal{R} = 32.50$ decreasing to $t_{\text{amp}} = 47.9$ for $\mathcal{R} \gtrsim 75$ (t_{amp} is dimensionless in the advection–diffusion scalings of Sec. II). Neither this bound, nor other estimates for the onset of convection based on particular initial conditions (for example, $t_{\text{amp}} = 75$ for a "white noise" initial condition[11]) or approximate techniques (for example, $t_{\text{amp}} = 146$ for a "dominant-mode" analysis[12]) have been verified experimentally.

Finally, a number of computational studies exist,[12–14] for which instability is sparked by spatial white noise in the initial concentration profile,[12] through spatial white noise in the porosity and permeability,[14] or by numerical round-off error alone.[13] Descriptions have primarily focused on relatively early times (before fingers hit the base). Onset times (as measured by flux deviation) range

from[13] $t_{\text{flux}} = 500$ to[14] $t_{\text{flux}} = 3670$. A steady flux regime was identified by Pau *et al.*[14] in which $\mathcal{S} = 0.017$ to 0.018 independent of $\mathcal{R}$.

Here we build a detailed description of convective dynamics and characterize several global measures from inception up to 65% saturation. In particular, we describe the flux throughout: initially it decays diffusively as $1/\sqrt{t}$, before arriving at a local minimum at the convective flux-onset, growing again to a local maximum, and then gradually decaying. We present a new theory for the flux shortly after convective fingers impact the layer bottom based on a Howard-style phenomenological model[15,16] and find it closely matches observations. Our experimental system permits easy and detailed inference of concentration profiles and we use this to present further global measures of the flow: the horizontally averaged concentration profile, from which we justify the Howard approach, and the amplitude used in theoretical studies of onset. The latter provides a first experimental confirmation of such studies, showing that the lower bound[10] is reasonably tight.

We start by describing the relevant scalings for the problem in Sec. II and then introduce the experimental setup in Sec. III. We then describe results for an experiment without convection in Sec. IV, observing close agreement with an error function similarity profile. This serves as a check against theory while also allowing us to infer the diffusivity D. In Sec. V, we describe a convection experiment from first contact through to almost complete saturation and quantify global measures and local properties of the flow for a range of Rayleigh numbers. Finally, in Sec. VI, we summarize our findings into a delineation and detailed description of the distinct convective regimes. We close with a brief discussion of how to relate our principal results to realistic CO_2-sequestration conditions.

II. LENGTH AND TIME SCALES

The primary physical processes in CO_2-dissolution are advection and linear diffusion of solute at a relatively low concentration (Péclet numbers are 10^{-6} to 10^{-3} in realistic formations and so Taylor dispersion is negligible[10]). Ignoring heterogeneity and secondary processes such as possible geochemical changes, this simple system has just a few relevant scales. We focus briefly on these scales here and identify their relative importance.

The relevant velocity scale is that with which a fully saturated parcel falls in an otherwise unsaturated medium,

$$\mathcal{U} = K\,\Delta\rho g/\mu,$$

while the two relevant length-scales are the distance over which advection and diffusion balance,

$$\mathcal{L} = \phi D/\mathcal{U},$$

and the layer thickness H. The three time-scales are (i) the time for advection or diffusion over the characteristic distance $\mathcal{L}$, $T_{\mathcal{L}} = \phi\mathcal{L}/\mathcal{U}$; (ii) the time for advection over the whole domain, $T_H = \phi H/\mathcal{U}$; and (iii) the time for diffusion over the whole domain, $T_D = H^2/D$.

At early times, when convection is localized close to the $KMnO_4$-water interface and away from the lower boundary, the layer thickness is irrelevant and the important scales are $\mathcal{L}$ and $T_{\mathcal{L}}$. We denote quantities scaled by this combination by subscript $\mathcal{L}$ and refer to them as the *advection–diffusion scalings*. We use the concentration at saturation c_{sat} to rescale the concentration field.

In contrast, at late times, after convective fingers have impacted the base, the scales H and T_H become increasingly important. We denote quantities non-dimensionalized by this combination by subscript H and refer to them as the *layer-thickness scalings*. We again use c_{sat} to rescale the concentration field.

The only dimensionless parameter is the ratio of the two length-scales $H/\mathcal{L}$, which is readily seen to equal the Rayleigh number $\mathcal{R}$ given in Eq. (1). In the advection–diffusion scalings, the Rayleigh number is the dimensionless layer thickness. Thus at early times, when $KMnO_4$ is far from the bottom boundary, we anticipate that behavior should be universal (parameter-independent) in the advection–diffusion framework. In the layer-thickness scalings relevant later, the Rayleigh number acts as a dimensionless inverse diffusivity.

Neither of our combinations correspond to the classical choice of scales H and T_D; indeed the classical combination does not allow for a good collapse of the data in any regime. We suggest that the

time-scale of diffusion over the layer thickness is irrelevant in convection and only appropriate for thin layers, where diffusion always dominates and convection is limited or impossible, or for very long times after convection has ceased (see also Hidalgo and Carrera[17] and Slim and Ramakrishnan[10]).

III. EXPERIMENTAL SETUP

Our experimental design was guided by a few key objectives: (i) finding a good mimic for CO_2, with a relatively low solubility, a relatively low excess density, and a linear dependence of density on dissolved concentration; (ii) easy visualization; (iii) observation of onset, in other words a sufficiently long diffusive regime before convection starts; and (iv) minimizing three-dimensional effects such as Taylor dispersion.

To meet these requirements, we used $KMnO_4$ in water as an analog for CO_2 in brine, with mass fraction at saturation $w_{\text{sat}} = 0.067$ and $\Delta\rho = 46$ kg m^{-3} (interpolated to the experimental ambient temperature of 23.4 °C from the relations given by Soehnel and Novotny[18]) compared to[19] w_{sat} up to 0.07 and $\Delta\rho$ up to 30 kg m^{-3} for CO_2 at reservoir conditions. We inferred concentrations to high accuracy and resolution from transmitted light intensity motivated by the Beer–Lambert law. The experiments were performed in almost horizontal ($0.1^\circ - 0.3^\circ$ inclination) Hele–Shaw cells to reduce the effective gravity and slow the dynamics so that onset of convection took tens of minutes. To limit three-dimensional effects, we ensured the gap d satisfied $d \lesssim 2\mathcal{L}$. We can approximate the combined effect of diffusion and dispersion in our system by the Taylor–Aris dispersion coefficient[20] for (symmetric) flow in a planar channel, $D + (1/210)(d/\mathcal{L})^2 D$ in our nomenclature, taking the average channel speed as the extremal value $\mathcal{U}$. When $d \lesssim 2\mathcal{L}$, diffusion significantly dominates dispersion. In the closely related problem of miscible Rayleigh–Taylor fingering in a vertical Hele–Shaw cell, Fernandez *et al.*[8] show experimentally and theoretically that $d \lesssim 10\mathcal{L}$ is required for diffusion to dominate dispersion. For our tilted cell, the restriction is presumably tighter owing to a counter-flow across the gap being easier to establish.

Our experimental setup is shown in Figure 1. The cell comprised two soda-lime glass plates 9.4 mm thick and $250 \pm 10\mu$m apart, with the gap maintained by precision brass shims along the sidewalls. The lower plate had a short strip of thinner glass attached to its top. The top of the upper plate was aligned with the top of this attachment to form a well with a depth of 5 mm and height of 12 mm. A fine, 316 stainless steel mesh of nominal screen size 37μm was placed in this well to hold $KMnO_4$ particles. The lower glass plate had a sharp edge in contact with the mesh (indicated as "sharp" in Figure 1(b)). This interface between the $KMnO_4$ particles and convection domain was effectively impermeable to convective fluid flow. The cell heights used were 38, 89, and 190 mm and the width was 280 mm.

Potassium permanganate was inserted in the well, to a layer thickness of at least 5 mm, as a barely wet paste to ensure neither particles nor solution would penetrate beyond the mesh during assembly. The paste was pressed down firmly into the well and left to dry in a fume hood for at least four hours. The remainder of the well was then filled with modeling clay and the whole cell sealed with silicone along the edges, except for a small air release on the opposite side of the water inlet (see Figure 1(a)).

To start an experiment, the cell was placed on three supports, one fixed and two adjustable through micrometers. The cell was horizontally levelled to within 0.02° using a Starrett 98 precision level and then the micrometer controlling the lower support (labelled 1 in Figure 1) adjusted to achieve the desired angle. The cell was then removed from the supports to fill with de-ionized water. This was done with the cell oriented vertically on the short edge having the water inlet, with water injected over a period of 1–2 min, ensuring the mesh and $KMnO_4$ wet fully. Once the cell was filled, the air release was sealed with vacuum grease. This seal appeared sufficient to avoid significant evaporative losses over the several-day duration of an experiment.

The cell was then returned to the supports, ensuring no change in the inclination occurred. Data collection then began, with an LED light tablet illuminating the cell from below and a Nikon D90 digital SLR (single lens reflex) camera collecting images from above. The data acquisition rate was a four-image burst every 60 s at early times and every 300 s at late times. The four images were averaged to reduce pixel noise. The camera, LED tablet, and supports were held in place rigidly

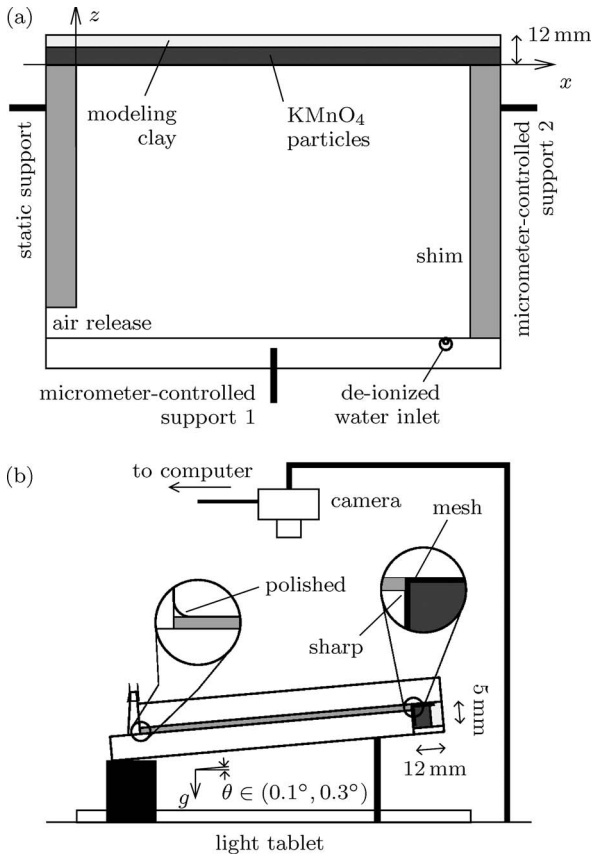

FIG. 1. (a) Plan view of the Hele–Shaw cell and (b) side view of the complete experimental setup (not to scale).

so that their relative positions were fixed. The entire apparatus was enclosed in a shroud to reduce background light and air currents (the latter to reduce temperature variations). Owing to sensitivity of the saturation concentration and excess density on temperature, we also recorded spot values of the temperature on the upper plate. The temperature was found to be $23.4 \pm 0.5\,^{\circ}\mathrm{C}$ (with the variation occurring within an experiment).

Table I gives the parameters for each experiment (the height of the cell and the angle to the horizontal) together with the scales $\mathcal{L}$, $T_{\mathcal{L}}$, and T_H, and the parameter $\mathcal{R}$.

A. Intensity–concentration calibration

Our goal was to characterize the spatio-temporal $KMnO_4$ concentration in the Hele–Shaw cell. To do so, we calibrated the concentration of $KMnO_4$ to the transmitted light intensity, averaging 16 images of the cell containing a prescribed-concentration solution. To account for inevitable minor spatial inhomogeneity in the light tablet's intensity, each averaged image was divided pixel-by-pixel by the corresponding pure-water image, thus providing a uniform value across the cell to within pixel noise. Extracted red, green, and blue channel values are shown in Figure 2. To infer low concentrations, we used the green channel (mass fraction $w < 0.006$); for higher concentrations we used the red channel. Sensitivity in the red channel at very high concentrations ($w > 0.04$) is limited and our accuracy is reduced. The error in the inferred concentration is less than 2.5% for $w < 0.04$. For $w > 0.04$ it increases to about 10%. Fortunately, only relatively small areas of the cell have such high concentration.

We note that the blue channel appears to be the best choice for higher concentrations; however, during an experiment this channel gradually reduced in intensity because of a slight but progressive rust-colored staining of the glass. The red and green channels appeared unaffected by this. At the

TABLE I. Experiment names, symbols, and parameters. Symbols are (sd) for short-dashed, (ld) for long-dashed, and (s) for solid. Errors in θ are $\pm 0.02^\circ$ and in H are ± 1 mm. To evaluate $\mathcal{L}$, $T_\mathcal{L}$, T_H, and $\mathcal{R}$, we take $D = 1.65 \times 10^{-9}$ m^2 s^{-1}, $\Delta\rho = 46$ kg m^{-3}, and $K = d^2/12 = 5.2 \times 10^{-9}$ m^2 as described in Secs. III and IV, together with $g = 9.81$ m s^{-1} and $\mu = 9.2 \times 10^{-4}$ Pa s. Errors in $\mathcal{L}$ and $T_\mathcal{L}$ are approximately 20%, 10%, and 7% for angles 0.11°, 0.21°, and 0.33°, respectively (principally due to the error in θ). Errors in T_H are twice this percentage. Asterisks (*) denote experiments with a small bubble at the interface.

	Sym	θ (deg)	H (mm)	$\mathcal{L}$ (μm)	$T_\mathcal{L}$ (s)	T_H (s)	$\mathcal{R}$
Dec13	s	0	190				
Dec07*	sd[a]	0.11	38	330	67	7700	110
Jan14*	sd[a]	0.11	38	330	67	7700	110
Jan06	s[a]	0.11	190	330	67	38 000	570
Dec29	sd[b]	0.21	38	180	19	4100	220
Dec18*	ld[b]	0.21	89	180	19	9500	510
Dec21	s[b]	0.21	190	180	19	20 000	1100
Dec22	sd[c]	0.33	38	110	7.6	2600	340
Jan11	ld[c]	0.33	89	110	7.6	6000	790
Dec30*	s[c]	0.33	190	110	7.6	13 000	1700

[a]Bold red online/bold print.
[b]Green online/light gray print.
[c]Blue online/dark gray print.

end of each experiment, the cell was disassembled and the staining readily removed with hydrogen peroxide.

To calculate the local concentration $c = \rho(w)w$ (as a mass of solute per unit volume of solution) and hence the total dissolved mass and dissolution flux, we assume the system is relatively dilute and take $\rho(w) = \rho(0)$. This resulted in an error of at most 3% in the mass in the longest-running experiments (less than the error due to lack of sensitivity in the concentration near saturation) and a negligible error in the flux. We opted for this because the error is insignificant and the mass fraction very marginally gives the better fit to the error function discussed in Sec. IV.

B. Limitations

A few limitations arose in our setup that we were unable to correct for. Bubbles would occasionally form on the mesh, even though it is nominally hydrophilic. If this occurred, then even for small bubbles the concentration field could be locally distorted away from the one-dimensional pure diffusion profile. Such experiments are marked with an asterisk in Table I. In these, behavior after onset appeared consistent with that for other experiments, however amplitudes (see Sec. IV A and Sec. V A 1) could not be obtained reliably. A second concern is the role of the corners in the

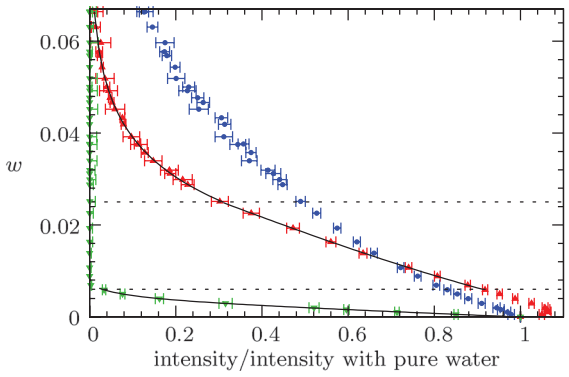

FIG. 2. The red (▲), green (▼), and blue (●) channel concentration–intensity relationships, together with the curve fits used.

Hele–Shaw cell. On the side that was at the bottom during filling, a larger pool of high concentration $KMnO_4$ solution could collect, while on the side that was at the top during filling, imperfect filling into the corner could result in a slight lag of the concentration profile. Finally, once high concentration fluid reached the bottom of the cell, bubbles would appear there. We speculate that this resulted from air trapped in the polish-groove of the upper plate (labelled "polished" in Figure 1(b)) balling up in response to the increase in surface tension.

IV. THE PURELY DIFFUSIVE STATE

We first describe a horizontal, pure-diffusion experiment where we compare the observed concentration profile with the analytic solution to check for non-linear diffusion and to infer the diffusivity.

Let z be the coordinate perpendicular to the $KMnO_4$-water boundary, directed into the $KMnO_4$ and with origin on the boundary. Then the pure Fickian diffusion profile following the step-change in concentration at the boundary at time $t = 0$ is

$$c_{\text{diff}} = c_{\text{sat}}[1 + \text{erf}(z/2\sqrt{Dt})],\ z < 0 \tag{3}$$

for constant diffusivity. The corresponding total dissolved mass per unit area of $KMnO_4$-water interface $m(t)$ (for brevity, we henceforth omit to state "per unit area," taking it as understood) and dissolution mass flux $F(t)$ are

$$m = \int_{-H}^{0} c_{\text{diff}}\,\text{dz} = 2\text{c}_{\text{sat}}\sqrt{\text{Dt}/\pi}, \tag{4a}$$

$$F = D\frac{\partial c_{\text{diff}}}{\partial z}\bigg|_{z=0} = c_{\text{sat}}\sqrt{D/(\pi t)}, \tag{4b}$$

respectively. Later, in the convection experiments, we will use the definitions $m = \int_V c\,\text{dV/W}$, where V is the volume of the cell and W its cross-sectional area, and $F = \text{dm/dt}$ to estimate the dissolved mass and dissolution flux.

Figure 3 shows the concentration profile along a z-transect of the cell at times from 5 min to 5 days after initial $KMnO_4$-water contact, together with the total dissolved mass. Fitting the function $f(t) = 2\sqrt{Dt/\pi}$ to the latter allows us to infer a diffusivity $D = 1.65 \pm 0.05 \times 10^{-9}\ \text{m}^2\ \text{s}^{-1}$. Here we take the inception time to be when the dissolved mass extrapolates to zero. This is in close agreement with the time of filling; however, because the filling process takes a finite time and introduces an anomalous initial dissolved mass of $KMnO_4$, we prefer to use the extrapolated time.

Using this value for D, we compare the observed concentration profile with Eq. (3) in Figures 3(a) and 3(b). We find excellent agreement, except at very high concentrations $c > 0.05$ where red-channel sensitivity is diminished and our accuracy is concomitantly reduced. This suggests that nonlinear diffusion is unimportant. The diffusivity obtained is in excellent agreement with the Nernst formula prediction[21] based on electrical neutrality of a simple salt at infinite dilution, $D = 1.70 \pm 0.02 \times 10^{-9}\ \text{m}^2\ \text{s}^{-1}$ at 23.4 °C (adjusting the value of $1.78 \times 10^{-9}\ \text{m}^2\ \text{s}^{-1}$ at 25 °C to ambient experimental temperatures). It is also broadly consistent with literature values, but surprisingly contradicts previous suggestions of a strong concentration dependence.[22,23]

A. Amplitude of the concentration field

To quantify the approach to, or deviation from, the pure-diffusion solution Eq. (3), we plot the perturbation amplitude in Figure 3(d). This is measured as

$$A(t) = \frac{1}{W}\int_V (c - c_{\text{diff}})^2\,\text{dV}, \tag{5}$$

the mean-square of the difference between the observed concentration profile and the theoretical solution associated with pure diffusion. Here again we take the initial time as the time at which the dissolved mass extrapolates to zero; using the time of starting to fill the cell or the time-stamp of

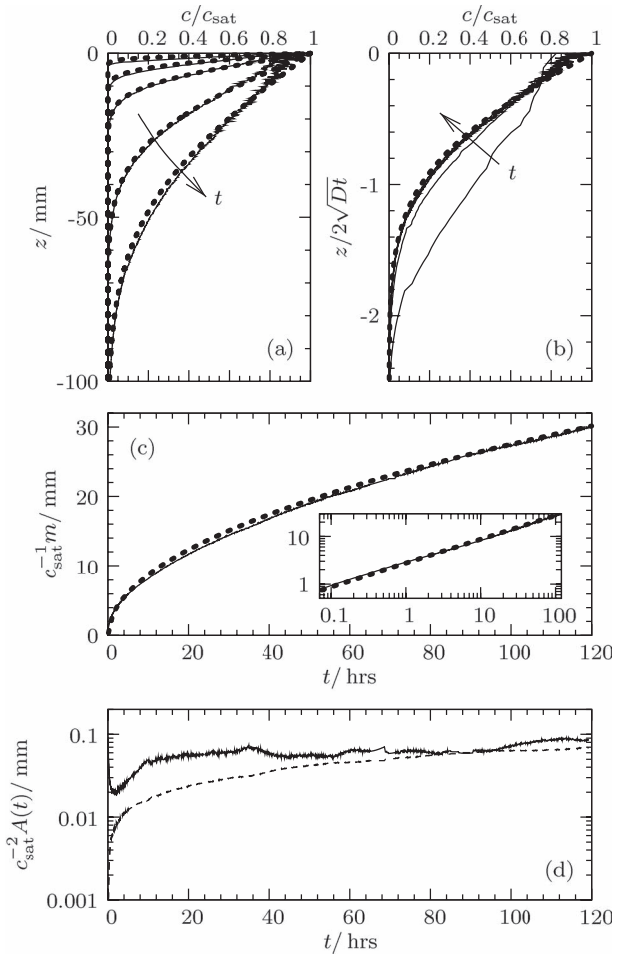

FIG. 3. Horizontal, pure diffusion experiment. The concentration profile along a z-transect for times $t \approx 5$ min, 1 h, 5 h, 38.5 h, and 120 h in (a) dimensional and (b) similarity form. (c) Dissolved mass per unit interfacial-area. In (a)–(c), the thin solid curves are experimental results and the bold dotted curves are the analytic pure diffusion solutions Eqs. (4) and (3). (d) Amplitude of perturbation away from pure diffusion (solid curve) together with an estimate of the measurement-error amplitude (dashed curve).

the first recorded image does not perceptibly alter the plot. There are two sources of amplitude: the actual difference $c - c_{\rm diff}$ and the measurement error in c. The dashed curve in the plot provides an estimate of the measurement-error contribution to the amplitude based on the error in the inferred concentration at each pixel. This error grows commensurately with the extent of the diffusion layer.

We observe an initial rapid decay of the amplitude during which the observed profile approaches the error function solution ever more closely. After about 1.5–2 h, the amplitude increases by a factor of about 2.5 before leveling off. We attribute this partly to the solution taking up a larger fraction of the cell, and thus more measurement error contributing, and partly to edge effects (the diffusion layer profile is slightly polluted in the two upper corners). This amplification is significantly less than observed in the convection experiments in Sec. V A 1.

In summary, we see that the error function profile for pure, linear, Fickian diffusion is very well reproduced in a horizontal experiment, with a diffusivity in good agreement with the Nernst formula.

V. CONVECTIVE FLOW

While diffusion is the dominant transport mechanism when the Hele–Shaw cell is horizontal, a very small tilt (of order $0.1^\circ - 0.3^\circ$) qualitatively changes the dynamics: then, following a transient

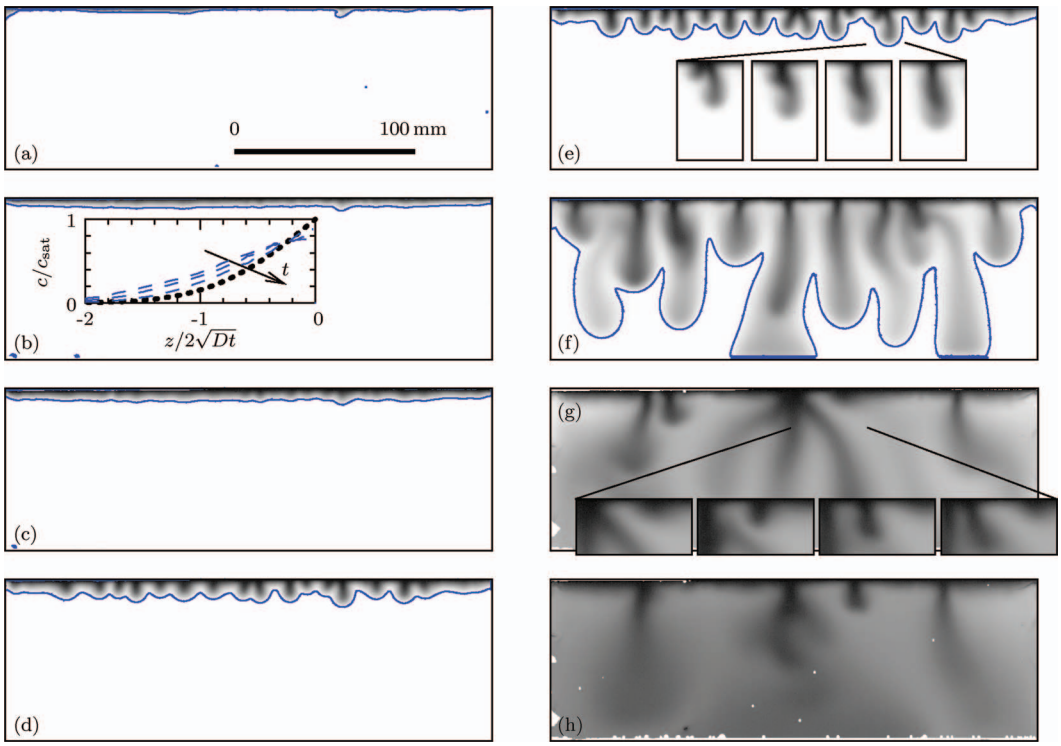

FIG. 4. "Jan11" convection experiment. Snapshots of the concentration field at times t ($t_{\mathcal{L}}$, t_H) after inception (a) 155 s (12, 0.016), (b) 20 min (160, 0.20), (c) 40 min (320, 0.40), (d) 90 min (710, 0.90), (e) 2 h (960, 1.2), (f) 8 h 15 min (3900, 4.9), (g) 25 h 15 min (12 000, 15), and (h) 45 h (21 000, 27). Solid curves in (a)–(f) are the $0.05c_{sat}$ contour. Insets show in (b) a vertical concentration slice at various times (thin solid curves) together with the analytic solution Eq. (3) (bold dotted curve), in (e) an early merger (at intervals of approximately 15 min, $120_{\mathcal{L}}$, 0.15_H), and in (g) a merger of a reinitiated finger (at intervals of 1 h, $470_{\mathcal{L}}$, 0.60_H). The solid curves are the $0.05c_{sat}$ contour. White spots are air bubbles (except along the left boundary where the camera was obscured).

diffusively dominated regime, we see convection. Before quantifying and analyzing local details and global measures across all experiments, we first describe the behavior in an exemplar experiment at a relatively high Rayleigh number of $\mathcal{R} = 790$. Figure 4 shows an image sequence depicting the evolution from almost first contact between the $KMnO_4$ and water to an average concentration of $0.65c_{sat}$ over three days.

The first image shows the initial concentration distribution. It is perturbed weakly at relatively long wavelength by inhomogeneities introduced during filling. This initial perturbation is rapidly smoothed away by diffusion (Figure 4(b)), and the resulting profile appears almost independent of the cross-cell coordinate x and is reasonably well described by the error-function solution Eq. (3) (inset to Figure 4(b)). Eventually, a hint of corrugations appears in the diffusion layer (Figure 4(c)) with a relatively uniform wavelength. These nascent fingers grow and become clearly defined (Figure 4(d)).

During this initial growth stage, the fingers grow independently of one another and propagate vertically at the same speed with little lateral motion. However, gradually fingers begin to interact (Figure 4(e)). The tips continue to propagate straight downwards, but the roots start to migrate towards one another. Eventually pairs of roots merge and the fingers zip together. If one finger is substantially shorter than the other, then it may be subsumed completely (inset to Figure 4(e)), or one of the fingers may channel the majority of the flow while the other is starved and gradually diffuses away. This process then repeats for subsequent merging events (up to five generations in this example). Occasionally, three fingers merge. We suggest that mergers occur when fingers reach a length commensurate with their spacing and their velocity fields start to interact. When a pair of fingers are close together, the return upflow generated by one finger is opposed by the downflow

generated by its neighbor. If a pair is slightly closer to each other than to their neighbors on either side, then less upwelling fresh fluid can penetrate between them than flows on either side. The fresh fluid rising up outside the pair rises up to the interface, where it spreads laterally and pushes the pair together.

Eventually, the first fingers impact the base of the cell (Figure 4(f)) and spread along it locally as a gravity current of dense fluid, leading to gradual saturation with $KMnO_4$.

Thus far the flow has evolved as a series of merging events between the fingers initiated at the onset of convection, with the elongating fingers progressively becoming more widely spaced. The fingers themselves become increasingly dishevelled through interactions; however, between finger roots there is a relatively uniform diffusive boundary layer. Eventually, mergers of primary fingers stops. However, reinitiations begin to occur between primary fingers (Figure 4(g)). The new finger forms as a growing bulge on the boundary layer between primary fingers and propagates into and merges with a primary finger at speeds between 0.9 and 2μm s^{-1}. Multiple generations of reinitiation and merging can occur between the same primary fingers. We suggest that reinitiation events commence when the inter-finger spacing is such that the time taken to traverse the distance between upwelling and downwelling is enough for perturbations to grow to macroscopic size. The complete history of finger initiation, merging, and reinitiation is shown in a space–time plot in Figure 5(a) for a slice 4 mm beneath the $KMnO_4$-water interface.

As the layer saturates, the intensity of convection is reduced, however some motion, finger reinitiation, and merging continues (Figure 4(h)).

For other inclination angles and cell sizes, the observed behavior is similar; for smaller (larger) angles, the dynamics are slower (faster) and fingers fatter (skinnier) in such a way that, on rescaling using the advection–diffusion scales $\mathcal{L}$ and $T_{\mathcal{L}}$, the dynamical behavior appears identical at early times across all experiments. How much of the behavior at later times are observed depends on the dimensionless layer thickness $\mathcal{R}$, effectively determining how much of the dynamics can be accommodated before the fingers impact the base. For the lowest $\mathcal{R}$, we observed at most a single generation of mergers, while for increasing $\mathcal{R}$ we see multiple mergers; for $\mathcal{R} \gtrsim 300$, we begin to see reinitiation events.[24]

A. Global measures of convection

Turning to quantitative measures, we plot the amplitude, dissolution flux, total dissolved mass, and horizontally averaged concentration profile against time for the exemplar experiment described above in Figure 5.

1. Amplitude

The amplitude (the mean-square difference between the observed concentration profile and that of pure diffusion) is again calculated according to Eq. (5) as described for the pure diffusion experiment in Sec. IV A. Since amplitude growth captures the formation of incipient fingers, it provides an early indicator of convection. Initially the amplitude drops rapidly before reaching a local minimum after approximately 20 min. Through this time, the profile conforms increasingly to the error function (inset to Figure 4(b)), while shortly afterwards, corrugations become visible. The amplitude then starts to grow quasi-exponentially, corresponding to the formation and growth of fingers. A sudden reduction in the growth rate occurs after about 150 min, corresponding to nonlinear amplitude saturation (in the sense of perturbations interacting). This occurs well before fingers impact the base.

Figure 6 shows the evolution of the amplitude for all experiments in which no significant bubbles were present at the interface. (Bubbles at the interface, occurring in experiments marked with an asterisk in Table I, result in a local lack of solute and so the profile does not adjust to the x-independent pure diffusion solution everywhere, polluting this measure of onset.) Although the time of minimum amplitude varies widely in dimensional units, using the advection–diffusion scalings, we find that the transition time from diffusion to convection collapses fairly well and occurs at $t_{\mathcal{L}} \approx 60$ to 160, close to the theoretical earliest possible onset time[10] of 47.9 and consistent

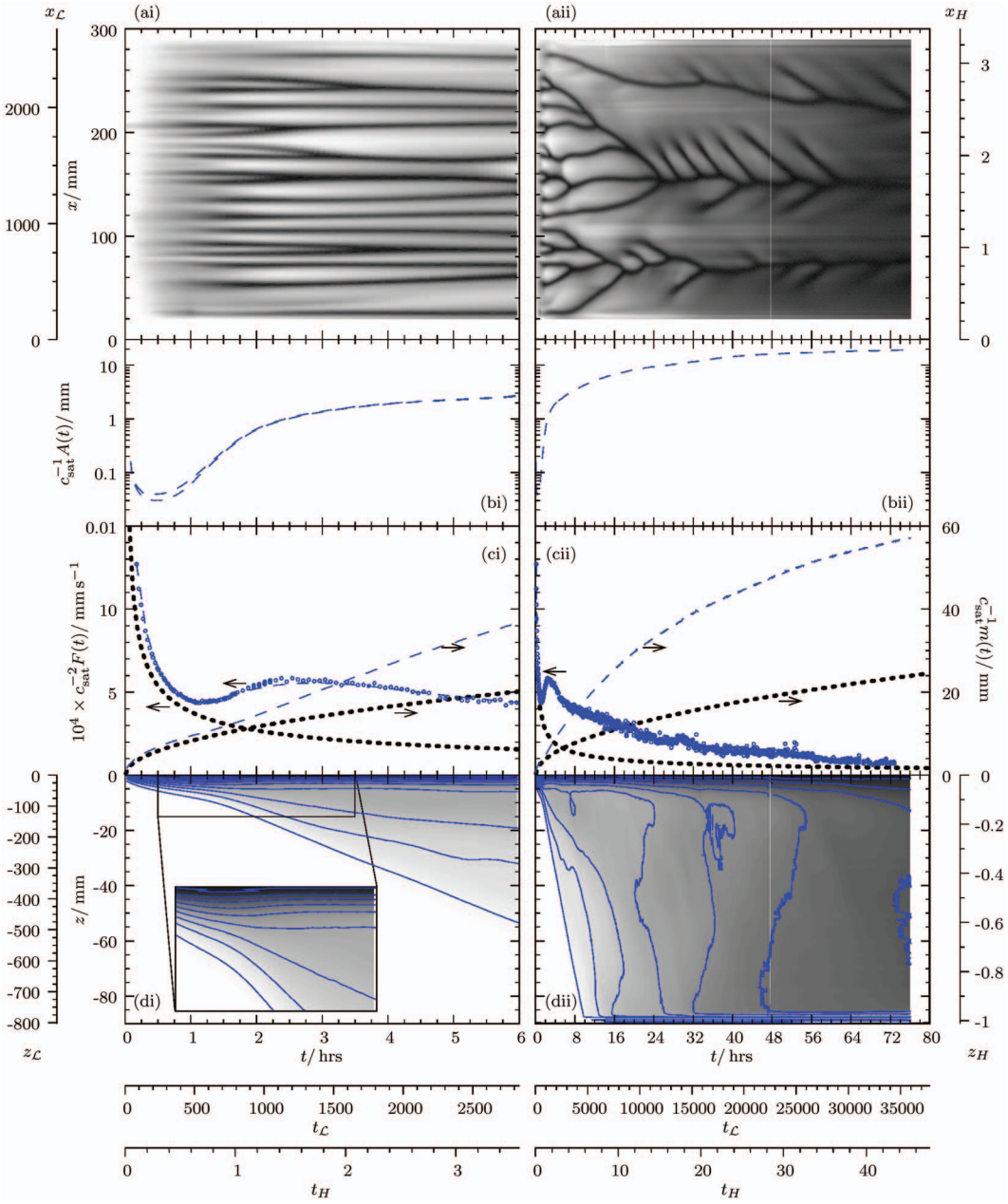

FIG. 5. "Jan11" convection experiment. Temporal behavior of (a) the concentration profile along the horizontal slice 4 mm below the $KMnO_4$-water interface, (b) the amplitude (the lower curve is a lower bound, subtracting the estimated measurement-error amplitude), (c) dissolution flux and dissolved mass per unit interfacial-area (the bold dotted curves are the analytic, pure diffusion solution Eqs. (4)), and (d) horizontally averaged concentration profile as a function of z. Contours in (d) are at intervals of $0.1c_{\rm sat}$ from $0.05c_{\rm sat}$. Left panels show early times; right panels show the full time history. For the flux, circles are raw time-differentiated mass data and the curve is a smooth interpolation.

with the "white noise" initial condition of Ennis-King and Paterson.[11] The quasi-exponential growth regime also collapses fairly well with the advection–diffusion scalings, with the growth rate being consistent with the value calculated for the "white noise" initial condition[11] and the maximum amplification of Rapaka *et al.*[25] (Figure 6(b)), albeit with a tangible dependence on the details of the initial perturbation. These experiments appear to be the first verification of the theoretical stability predictions for time-dependent, diffusively dominated base states.

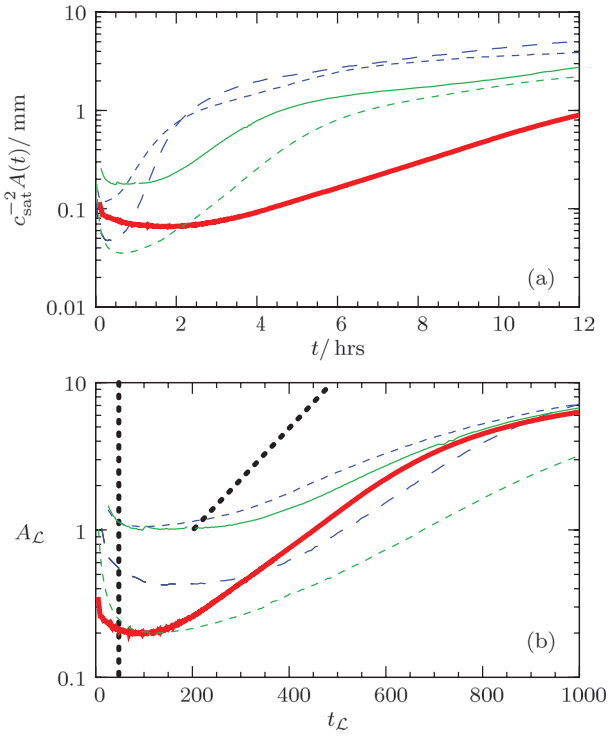

FIG. 6. Amplitude against time for all convection experiments without bubbles at the interface in (a) dimensional and (b) advection–diffusion forms. In (b), the bold dotted line at $t = 47.9$ is the theoretical lower bound on onset time. The second dotted line is proportional to $e^{0.008t_{\mathcal{L}}}$, an excellent fit to both the maximum amplification[25] across all horizontal wavenumbers and the growth of "white noise" initial conditions[11] for horizontal wavenumber $k_{\mathcal{L}} = 0.05$ and for $t_{\mathcal{L}} \gtrsim 200$ and $\mathcal{R} \geq 100$.

2. Flux

The quantity of greatest practical significance is the dissolution flux, shown in Figure 5(c) as a function of time for our exemplar experiment. Initially, the flux decays diffusively as $1/\sqrt{t}$. However after approximately 70 min, a rapid transition occurs and the flux begins to increase as convection brings fresher water close to the interface. This is after fingers have formed but before nonlinear amplitude saturation and well before fingers hit the bottom. The flux then briefly increases to a local maximum at 170 min, shortly after nonlinear amplitude saturation but still before fingers hit the base, before gradually decaying. The first mergers are roughly synchronous with this maximum.

Figure 7 shows the flux for all experiments in both dimensional and dimensionless forms, using both the advection–diffusion and layer-thickness scalings. The trends described in the previous paragraph carry over to all experiments; initially they all show a $1/\sqrt{t}$ decay before a sharp shift from this behavior associated with the onset of convection. The times for this shift are reasonably uniform when non-dimensionalized by the advection–diffusion scalings and occur at $t_{\mathcal{L}} \approx 400$ to 700. A flux increase then occurs to a local maximum at $t_{\mathcal{L}} \approx 800$ to 1400, before progressively decaying, maintaining a reasonable collapse with the advection–diffusion scalings for early times. We suggest that the remaining variability is due to variations in the initial perturbation and experimental error. At later times, the collapse becomes poor and a much better collapse is obtained with the layer-thickness scalings, beyond $t_H \approx 7$.

3. Horizontally averaged concentration field

To understand the flux better, we also consider the horizontally averaged concentration field, shown in Figure 5(d) for our exemplar experiment. For a short time, the profile appears purely diffusive, though after 70 to 80 min, the diffusive boundary layer starts to thin and dissolved $KMnO_4$ starts to extend further from the interface. This process happens as fingers drag contaminated

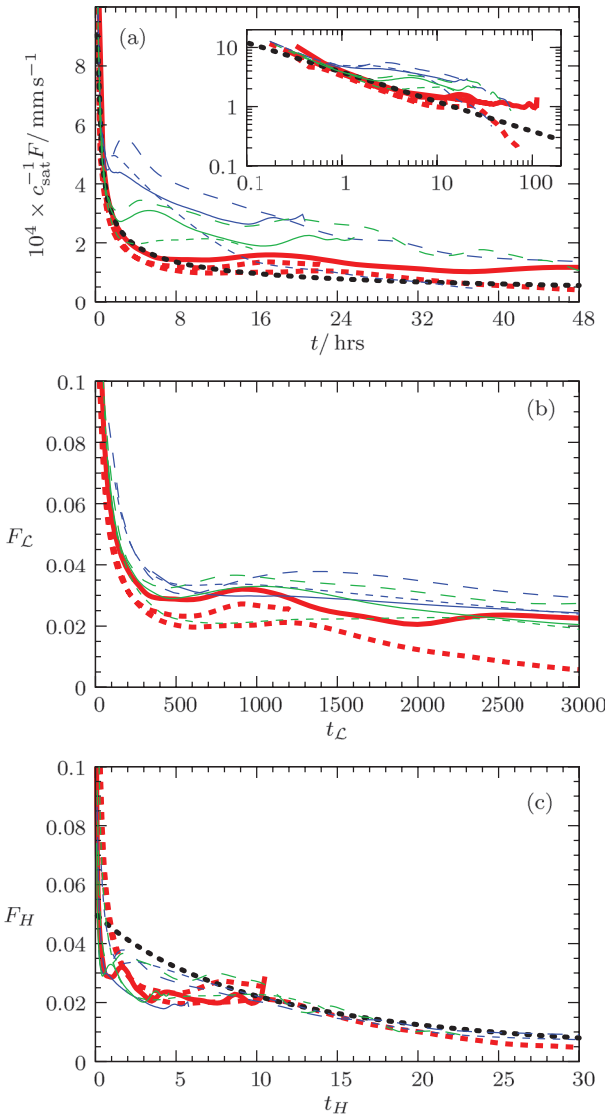

FIG. 7. Flux against time across all convection experiments in (a) dimensional, (b) advection–diffusion, and (c) layer-thickness formulations. In (a), the bold dotted curve is the analytic, pure diffusion solution Eq. (4b). In (c), the bold dotted curve is the late-time phenomenologically derived scaling Eq. (9c). Fluxes have been smoothed to improve readability.

water further from the interface and bring fresher water closer to the interface (observe also the lower concentration, lighter patches appearing in the space-time plot Figure 5(a) at around 100 to 200 min). The latter sharpens the effective boundary layer gradient at the interface and so increases the flux of $KMnO_4$. An overshoot in the flux is observed because it takes time for the fingers to amplify sufficiently to strip dense material from the interface effectively. While the fingers grow, the diffusion layer thickens beyond its unstable value (achieved at amplitude onset) so that the flux drops below what it would have been if fully developed fingers formed instantaneously. However once fingers are fully formed they strip this excess dense material from the interface to establish a thinner diffusive boundary layer between fingers, with a concomitant increase in the flux.

Eventually, the horizontally averaged concentration field at the bottom of the cell begins to increase when fingers first make impact there. The concentration is now slightly higher at the base as gravity currents spread along it. However gradually a profile is established in which the bulk of the cell has a z-independent horizontally averaged concentration with a boundary layer at the interface that progressively thickens (Figure 8).

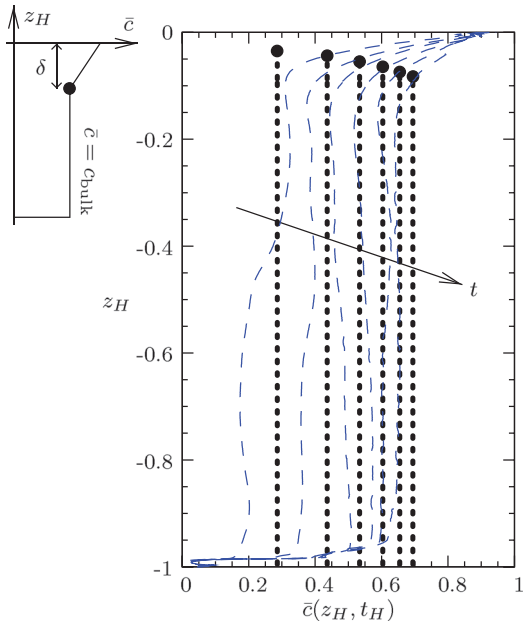

FIG. 8. Horizontally averaged concentration profile against vertical coordinate for the "Jan11" experiment at times $t = 13.5$, 26.0, 51.1, 63.6, and 76.1 h in the direction of the arrow ($t_H = 8.0$, 15, 30, 38, and 45). Fingers first impact the base of the cell at $t \approx 10$ h ($t_H \approx 6$). The bold dotted profiles are the bulk concentration estimates from the phenomenological relation Eq. (9a).

4. A minimal model for the flux

Using these last observations, we adapt the Howard phenomenology[15,16] for thermal convection to the time-dependent solutal-convection case and characterize the flux at late times. Using the layer-thickness scaled variables, we assume that the bulk of the fluid has a uniform concentration $c_{\text{bulk}}(t_H)$ and that there is an upper boundary layer with a linear concentration gradient and thickness $\delta(t_H)$ (see Figure 8 inset). Then the total dissolved mass is

$$m_H(t_H) = c_{\text{bulk}} + \frac{1}{2}\delta(1 - c_{\text{bulk}}) \tag{6}$$

and the flux into the system is

$$F_H(t_H) = \frac{1}{\mathcal{R}}\frac{1 - c_{\text{bulk}}}{\delta} = \frac{\mathrm{dm_H}}{\mathrm{dt_H}}. \tag{7}$$

A key physical ingredient of the theory is the assumption that the boundary layer always has critical thickness for convection: if the boundary layer is thinner, then it is stable and thickens by diffusion, whereas if the boundary layer is thicker, then perturbations grow, convective plumes strip away material, and it thins. Thus

$$\mathcal{R}(1 - c_{\text{bulk}})\delta = \mathcal{R}_c. \tag{8}$$

The value of $\mathcal{R}_c$ is not clearly defined in the analysis: a naïve estimate would be $\mathcal{R}_c = 4\pi^2$, the critical Rayleigh number for steady convection in a layer with impermeable boundaries and prescribed concentrations at top and bottom.[26] The analysis of Slim and Ramakrishnan[10] yields a minimum value $\mathcal{R}_c = 13.8$, with an error function profile for the boundary layer, however this does not account for upflow between fingers stabilizing the boundary layer. Here, we use the *ad hoc* value $\mathcal{R}_c = 20$, which agrees well with simulations for thermal convection in a porous medium.[16]

Combining Eqs. (6)–(8), we obtain the ordinary differential equation

$$\frac{\mathrm{dc_{bulk}}}{\mathrm{dt_H}} = \frac{1}{\mathcal{R}_c}(1 - c_{\text{bulk}})^2,$$

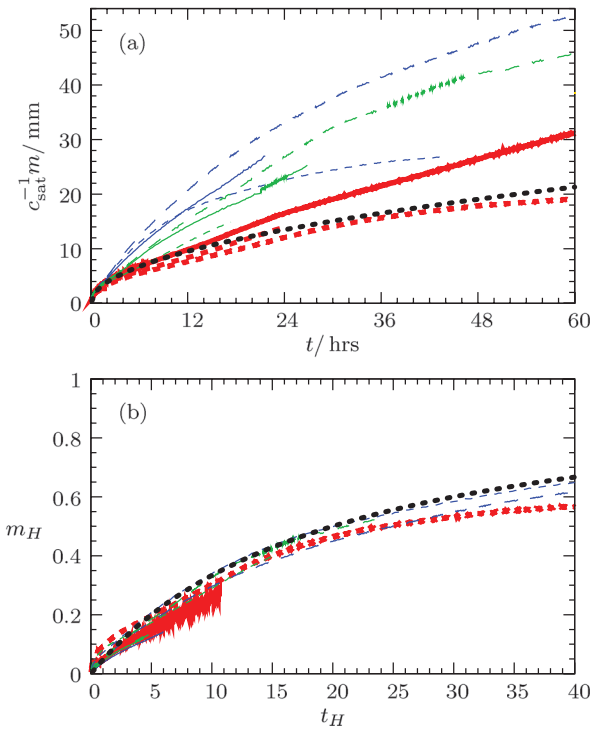

FIG. 9. Dissolved mass per unit interfacial-area against time across all convection experiments in (a) dimensional and (b) layer-thickness forms. The thick, dotted curve in (a) is the analytic, pure diffusion solution Eq. (4a) and in (b) is the late-time phenomenologically derived scaling Eq. (9d), omitting the $\mathcal{R}_c/2\mathcal{R}$ term.

with the solution

$$c_{\rm bulk} = \frac{t_H}{\mathcal{R}_c + t_H}, \tag{9a}$$

$$\delta = \frac{\mathcal{R}_c + t_H}{\mathcal{R}}, \tag{9b}$$

$$F_H = \frac{\mathcal{R}_c}{(\mathcal{R}_c + t_H)^2}, \tag{9c}$$

$$m_H = c_{\rm bulk} + \frac{\mathcal{R}_c}{2\mathcal{R}}. \tag{9d}$$

Here we have taken $c_{\rm bulk} = 0$ at $t_H = 0$. This provides a good description of the late-time flux (Figure 7(c)), the horizontally averaged concentration profile (Figure 8), and the total dissolved mass (Figure 9).

5. Landmark times

Figure 10 gives a summary of landmark times across all experiments in the two different scalings. We find the advection–diffusion scalings appropriately collapse the amplitude onset and nonlinear amplitude saturation and the flux minimum and maximum to within inter-experiment variability and measurement error. The flux maximum and first mergers (not plotted for clarity but occurring at $t_{\mathcal{L}} \approx 600$ to 1600) coincide to within variability and error. The layer-thickness scalings are, unsurprisingly, appropriate for times at which fingers extend halfway and the full height of the cell, and the average saturation reaching 50%. Fingers reach half-way down the cell at $t_H \approx 4$ and hit the bottom at $t_H \approx 7 \pm 2$. The latter is also when the flux begins to collapse better with the layer-thickness scalings. A saturation of 50% is reached at $t_H \approx 20$ to 25.

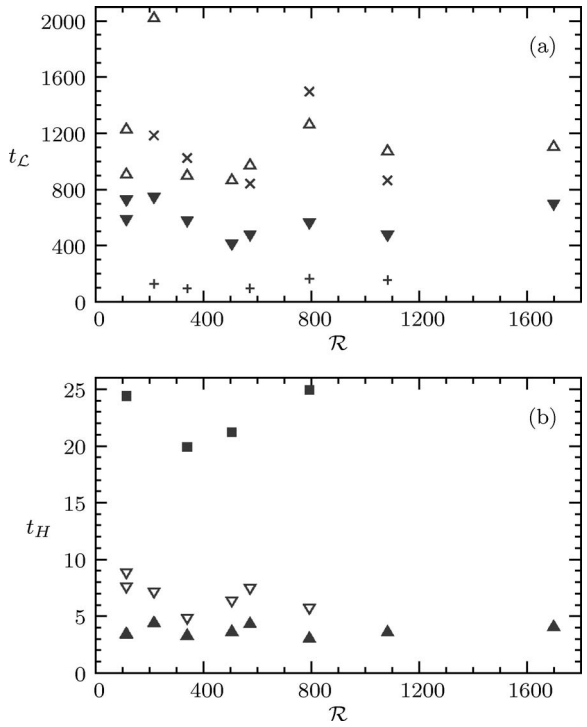

FIG. 10. Landmark times. (a) Amplitude onset (+), flux onset (▼), flux maximum (△), and nonlinear amplitude saturation (×) in advection–diffusion scalings. (b) Fingers half-way down the cell (▲), fingers impacting bottom (▽), and 50% average saturation (■) in layer-thickness scalings. Finger location measures are taken when the horizontally averaged concentration reaches $0.05c_{\text{sat}}$ at that location.

B. Local measures of convection: Wavelengths and finger velocities

Our discussion thus far has focused primarily on global variables. We now turn to smaller-scale features of the flow, starting with the wavelength defined as the average distance between concentration peaks. In Figure 11, we show the wavelength for all experiments using the advection–diffusion scalings. Initially, fingers have the relatively short wavelength $\lambda_{\mathcal{L}} \approx 60$ to 110, reasonably close to the stability theory prediction $\lambda_{\mathcal{L}} \approx 120$. Some of the experimental undershoot may result from incorrectly identifying small bumps as true fingers. This wavelength is set by a competition between horizontal diffusion smoothing short waves and insufficient dense material having

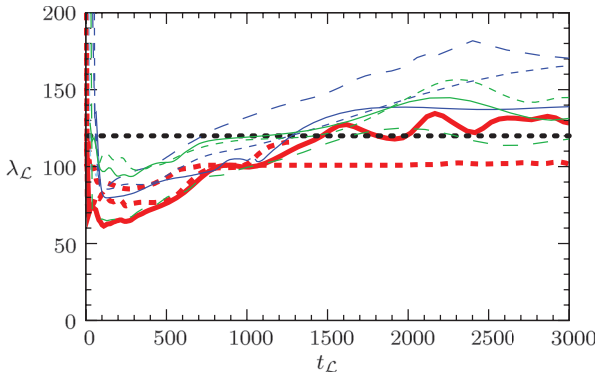

FIG. 11. Wavelength in time in the advection–diffusion framework across all convection experiments. The bold dotted curve is the stability theory prediction[10] $\lambda_{\mathcal{L}} \approx 120$. Experimental wavelengths are defined as the average distance between peaks on a horizontal slice 4 mm beneath the interface.

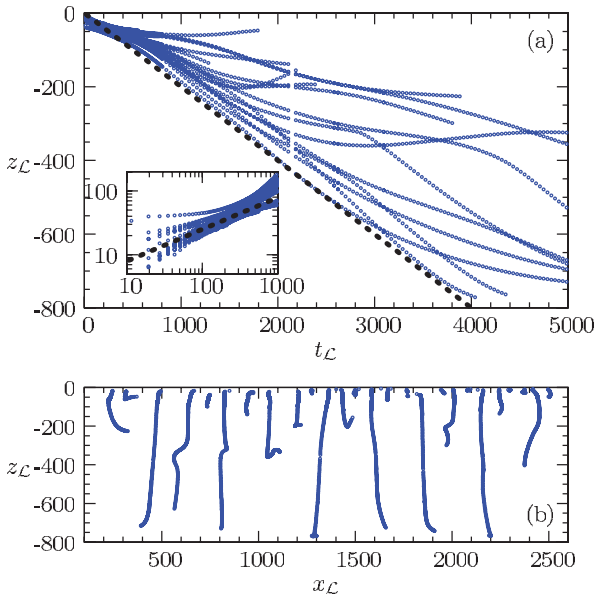

FIG. 12. Vertical fingertip locations against (a) time and (b) horizontal coordinate in the advection–diffusion framework for the "Jan 11" experiment. In (a), the bold dotted line is $z_{\mathcal{L}} = 0.2t_{\mathcal{L}}$; the inset shows the same plot logarithmically and includes the curve $z_{\mathcal{L}} = -2.5\sqrt{t_{\mathcal{L}}}$.

accumulated to drive long waves.[10] As has already been described, it subsequently coarsens through mergers.

In Figure 12, we also follow the behavior of the fingertips in the advection–diffusion scalings, defining the tips as local minima of the $0.05c_{\text{sat}}$ contour. Initially, all fingers behave similarly and fall in a diffusive fashion as approximately $z_{\mathcal{L}} = -(2.5 \pm 0.5)\sqrt{t_{\mathcal{L}}}$ until $t_{\mathcal{L}} \approx 600$, corresponding to the time of minimum flux. This further emphasizes that earlier behaviour is still primarily diffusive, superposed with relatively small amplitude perturbations. After this time, behaviors diverge, with some fingers accelerating and achieving an almost constant speed while others decelerate further and may even retreat. The fastest fingers descend with a speed of approximately $0.2_{\mathcal{L}}$ all the way to the bottom, often with surprisingly little retardation before impact. These pioneers have relatively little lateral motion (Figure 12(b)). In contrast, slower fingers are often significantly deflected; they may merge laterally with neighbors or retreat. In the advection–diffusion framework, the same scenario is observed for all experiments; in particular, the initial diffusive scaling and maximum velocity appear universal.

VI. SUMMARY AND CONCLUSIONS

We have presented a high spatial and temporal resolution experimental study of dissolution-driven convection in a Hele–Shaw cell from first contact between $KMnO_4$ solute and water solvent through to 65% saturation. We described dynamical details and quantified global measures throughout the evolution. Our work confirms features of earlier experimental and numerical studies, but also goes beyond them in providing details of the dynamics at both a local and global level in a single unifying, universal framework through the advection–diffusion scalings (based on the distance over which advection and diffusion balance) and shows that aspects of the behavior can be captured by a simple coarse-grained Howard-style model.

We can summarize our results into a discussion of six reasonably distinct regimes, shown schematically in Figure 13. The first four of these are understood in terms of the advection–diffusion scaling and the last is understood in terms of the layer-thickness scaling (in which the layer thickness is the dominant length scale). The scalings appropriate for the penultimate regime are as yet unclear.

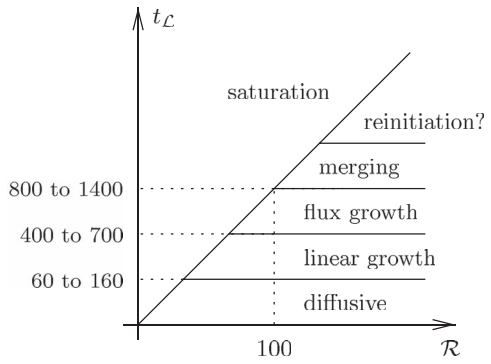

FIG. 13. Summary of the six distinct regimes as a function of Rayleigh number and advection–diffusion time.

1. Initially, there is a *diffusive regime* in which the concentration profile is close to a one-dimensional diffusive error function. The flux decays as $1/\sqrt{t}$.
2. When time in the advection–diffusion scalings satisfies $t_{\mathcal{L}} \approx 60$ to 160, the flow transitions to a *linear growth regime* in which the mean-square of the difference between the observed concentration profile and the error function starts to grow and rapidly achieves quasi-exponential growth. Convective fingers grow independently of one another with little or no lateral motion and tip positions evolve as $z_{\mathcal{L}} \approx -(2.5 \pm 0.5)\sqrt{t_{\mathcal{L}}}$. The time of transition, growth rate, and the observed wavelength $\lambda_{\mathcal{L}} \approx 60$ to 110 are in reasonable agreement with theoretical stability analyses.
3. The flow then enters a *flux growth regime* in which the flux begins to deviate significantly from pure diffusion at $t_{\mathcal{L}} \approx 400$ to 700 and grows to a local maximum at $t_{\mathcal{L}} \approx 800$ to 1400. Note that this flux-onset condition is intermediate between previously reported experimental results[4] and simulations.[12–14] This inherently nonlinear phenomenon does not occur until the fingers are well defined. Fingers begin to accelerate, however they still have little lateral motion.
4. The flow next transitions into a *merging regime*, with neighboring fingers zipping together from the root downwards, suggesting a secondary instability. The first mergers occur roughly concurrently with the flux maximum and can continue for at least five generations. During this regime the flux gradually decays.
5. Next, there is a *reinitiation regime*. Once primary fingers are sufficiently widely spaced, no further annihilation appears to occur, however new fingers form (reinitiate) between them. These immature fingers are rapidly swept into primary fingers by the intervening upflow. Subsequent reinitiations tend to occur further from the attracting primary than the first. This regime is qualitatively similar to that observed for classical thermal convection in a porous medium.[27,28] Throughout, the flux gradually decays. Unfortunately, we have limited data on this regime because we either did not run the relevant experiment to conclusion (the "Dec 30" experiment) or $\mathcal{R}$ was not large enough for this regime to be well-established prior to the bottom boundary influencing the dynamics.
6. After fingers impact the bottom, at $t_H \approx 7 \pm 2$, the flow enters a *saturating regime*. Beyond this time the layer-thickness scalings apply. Progressively the flow adjusts so that the horizontally averaged concentration field becomes vertically uniform in the bulk with a progressively broadening upper boundary layer. The decaying flux is now well-described by a modified Howard-style phenomenology.

The behavior described is universal across our experiments in the intrinsic advection–diffusion scalings (in which the layer thickness only appears as the dimensionless location of the lower boundary) until fingers impact the base, at which point the progression through the advection–diffusion regimes is interrupted. Thus how much of the picture is observed depends on $\mathcal{R}$, the dimensionless layer thickness, and single parameter of the problem. Our smaller $\mathcal{R}$ experiments barely reach the merging regime; the reinitiation regime is observed for $\mathcal{R} \gtrsim 300$.

A number of intriguing questions remain. Although we postulated explanations, why precisely does merging begin and end and why do reinitiations begin? Why does the coarse-grained Howard description work so well? How universal is the early collapse and when precisely do transitions between regimes occur and for which Rayleigh number are they observed? For larger $\mathcal{R}$ than we obtained, there is also the potential for further regimes between merging and saturating (which in turn might affect the nature of the saturating regime), such as the apparent constant flux regime observed[5,6,14] at very high $\mathcal{R}$.

Our setup provides an analog for dissolution-driven convection in an ideal, homogeneous porous medium. As such, it is expected to provide lower bounds on dissolution rates and upper bounds on time scales for the CO_2 dissolution process in a real, heterogeneous formation.[11,29,30] A result of particular interest is the phenomenological description of the flux, providing a first step towards a dissolution-rate parameterization for reservoir-scale simulators where convection is a sub-grid-scale process. However, in this application it is also necessary to understand how robust the results are in conjunction with concurrent supercritical CO_2 evolution, as well as the nature of the boundary dividing the two-phase region from the underlying convecting brine layer. Hence significant work is still required.

ACKNOWLEDGMENTS

We thank Schlumberger–Doll Research for financial support, and Scott Backhaus, R. E. Ecke, Sharon Gerbode, John Gregoire, and Shmuel Rubinstein for helpful discussions.

[1] *IPCC Special Report on Carbon Dioxide Capture and Storage*, edited by B. Metz, O. Davidson, H. C. de Coninck, M. Loos, and L. Meyer (Cambridge University Press, New York, 2005).
[2] G. J. Weir, S. P. White, and W. M. Kissling, "Reservoir storage and containment of greenhouse gases," Transp. Porous Media **23**, 37–60 (1996).
[3] E. Lindeberg and D. Wessel-Berg, "Vertical convection in an aquifer column under a gas cap of CO_2," Energy Convers. Manage. **38**, S229–S234 (1997).
[4] T. J. Kneafsey and K. Pruess, "Laboratory experiments and numerical simulation studies of convectively enhanced carbon dioxide dissolution," Energy Procedia **4**, 5114–5121 (2011).
[5] J. A. Neufeld, M. A. Hesse, A. Riaz, M. A. Hallworth, H. A. Tchelepi, and H. E. Huppert, "Convective dissolution of carbon dioxide in saline aquifers," Geophys. Res. Lett. **37**, L22404, doi:10.1029/2010GL044728 (2010).
[6] S. Backhaus, K. Turitsyn, and R. E. Ecke, "Convective instability and mass transport of diffusion layers in a Hele-Shaw geometry," Phys. Rev. Lett. **106**, 104501 (2011).
[7] R. Wooding, "Growth of fingers at an unstable diffusing interface in a porous medium or Hele-Shaw cell," J. Fluid Mech. **39**, 477–495 (1969).
[8] J. Fernandez, P. Kurowski, P. Petitjeans, and E. Meiburg, "Density-driven unstable flows of miscible fluids in a Hele-Shaw cell," J. Fluid Mech. **451**, 239–260 (2002).
[9] D. A. S. Rees, A. Selim, and J. P. Ennis-King, "The instability of unsteady boundary layers in porous media," in *Emerging Topics in Heat and Mass Transfer in Porous Media: From Bioengineering and Microelectronics to Nanotechnology*, Theory and Application of Transport in Porous Media, Vol. 22 (Springer, Dordrecht, 2008), pp. 85–110.
[10] A. C. Slim and T. S. Ramakrishnan, "Onset and cessation of time-dependent, dissolution-driven convection in porous media," Phys. Fluids **22**, 124103 (2010).
[11] J. Ennis-King and L. Paterson, "Role of convective mixing in the long-term storage of carbon dioxide in deep saline formations," SPE J. **10**, 349–356 (2005).
[12] A. Riaz, M. Hesse, H. A. Tchelepi, and F. M. Orr, "Onset of convection in a gravitationally unstable diffusive boundary layer in porous media," J. Fluid Mech. **548**, 87–111 (2006).
[13] H. Hassanzadeh, M. Pooladi-Darvish, and D. W. Keith, "Scaling behavior of convective mixing, with application to geological storage of CO_2," AIChE J. **53**, 1121–1131 (2007).
[14] G. S. H. Pau, J. B. Bell, K. Pruess, A. S. Almgren, M. J. Lijewski, and K. Zhang, "High-resolution simulation and characterization of density-driven flow in CO_2 storage in saline aquifers," Adv. Water Resour. **33**, 443–455 (2010).
[15] L. N. Howard, "Convection at high Rayleigh numbers," in *Applied Mechanics, Proceedings of 11th Congress of Applied Mathematics*, edited by H. Görtler (Springer, Berlin, 1964), pp. 1109–1115.
[16] C. R. Doering and P. Constantin, "Bounds for heat transport in a porous layer," J. Fluid Mech. **376**, 263–296 (1998).
[17] J. J. Hidalgo and J. Carrera, "Effect of dispersion on the onset of convection during CO_2 sequestration," J. Fluid Mech. **640**, 441–452 (2009).
[18] O. Söhnel and P. Novotný, *Densities of Aqueous Solutions of Inorganic Substances* (Elsevier, New York, 1985).
[19] J. E. García, "Fluid dynamics of carbon dioxide disposal into saline aquifers," Ph.D. dissertation (Lawrence Berkeley National Laboratory, 2003).
[20] A. C. Fowler, *Mathematical Models in the Applied Sciences* (Cambridge University Press, New York, 1997) p. 214.
[21] *CRC Handbook of Chemistry and Physics: A Ready-Reference Book of Chemical and Physical Data*, 91st ed., edited by D. R. Lide (CRC, Boca Raton, 2010), Chaps. 5–76.

[22] R. Fürth and E. Ullmann, "Zur physikalischen chemie der farbstoffe, V," Kolloid-Z. **41**, 304–310 (1927).
[23] G. Taylor, "Dispersion of soluble matter in solvent flowing slowly through a tube," Proc. R. Soc. London, Ser. A **219**, 186–203 (1953).
[24] For $\mathcal{R} = 340$ a small number of reinitiations are observed; for $\mathcal{R} = 110$ and 220 none were observed. Unfortunately, the experiment with $\mathcal{R} = 270$ was not run to saturation.
[25] S. Rapaka, S. Chen, R. J. Pawar, P. H. Stauffer, and D. Zhang, "Non-modal growth of perturbations in density-driven convection in porous media," J. Fluid Mech. **609**, 285–303 (2008).
[26] D. A. Nield and A. Bejan, *Convection in Porous Media* (Springer, New York, 2006).
[27] M. D. Graham and P. H. Steen, "Plume formation and resonant bifurcations in porous-media convection," J. Fluid Mech. **272**, 67–90 (1994).
[28] J. Otero, L. A. Dontcheva, H. Johnston, R. A. Worthing, A. Kurganov, G. Petrova, and C. R. Doering, "High-Rayleigh-number convection in a fluid-saturated porous layer," J. Fluid Mech. **500**, 263–281 (2004).
[29] C. P. Green and J. Ennis-King, "Effect of vertical heterogeneity on long-term migration of CO_2 in saline formations," Transp. Porous Media **82**, 31–47 (2010).
[30] R. Farajzadeh, P. Ranganathan, P. L. J. Zitha, and J. Bruining, "The effect of heterogeneity on the character of density-driven natural convection of CO_2 overlying a brine layer," Adv. Water Resour. **34**, 327–339 (2011).